Editors' Suggestion

Hourglass-type bulk Ni 3*d* band and Ce 4*f* Kondo resonance states in the potential topological Kondo semimetal CeNiSn via angle-resolved photoemission spectroscopy

Seungho Seong,[1] J. D. Denlinger,[2] Kyoo Kim,[3] B. I. Min,[4] Y. Ōnuki,[5] and J.-S. Kang[1,*]

[1]*Department of Physics, Catholic University of Korea, Bucheon 14662, Republic of Korea*
[2]*Lawrence Berkeley Laboratory, Berkeley, California 94720, USA*
[3]*Korea Atomic Energy Research Institute (KAERI), Daejeon 34057, Republic of Korea*
[4]*Department of Physics, Pohang University of Science and Technology, Pohang 37673, Republic of Korea*
[5]*RIKEN Center for Emergent Matter Science, Wako, Saitama 351-0198, Japan*

(Received 21 November 2022; accepted 15 February 2023; published 3 March 2023)

The electronic structure of CeNiSn, which is a potential topological Kondo insulator and a Dirac nodal-loop semimetal, has been investigated by employing temperature (T) dependent angle-resolved photoemission spectroscopy (ARPES). The Fermi surfaces (FSs) and the band structures of CeNiSn for three orthogonal crystallographic planes are measured, in which both the very dispersive bands and the flat bands are observed, having mainly the Ni 3*d* character and the Ce 4*f* character, respectively. The measured FSs and ARPES bands agree reasonably well with the density functional theory (DFT) calculations. The Fermi-edge (E_F) photon energy ($h\nu$) map along k_b ($= k_{(010)}$) shows that the metallic E_F-crossing states on the (010) surface have the three-dimensional character, suggesting that the observed E_F-crossing metallic states do not correspond to the topological surface states of the two-dimensional character. On the other hand, albeit weak, the features of the hourglass-type bulk band crossings are observed along SXS, with the energies and the slopes being similar to those predicted by the DFT calculations, supporting the Dirac semimetallic nature of CeNiSn. In T-dependent ARPES, the Ce 4*f* Kondo resonance states are clearly revealed at low T, which become much suppressed above ~80 K. This feature is consistent with the Kondo temperature of CeNiSn, estimated from its $\rho(T)$ data. This work demonstrates the importance of the coherent Kondo states in determining the topological properties of CeNiSn.

DOI: 10.1103/PhysRevB.107.125109

I. INTRODUCTION

Among various topological insulators [1,2], strongly correlated Kondo insulators are unique because they exhibit temperature (T) dependent topological phases [3,4]. The representative topological Kondo insulator (TKI) might be SmB_6 [3,4]. SmB_6 exhibits *bulk* insulating behavior below 50 K, and then a resistivity plateau at low T below 5 K, which is considered to originate from the topological surface state (TSS). Despite extensive experimental and theoretical studies on SmB_6, however, the TKI nature of SmB_6 is still controversial experimentally [5–11].

Recently, Ce-based Kondo insulator CeNiSn has been predicted to be a TKI theoretically, having the Möbius-twisted TSS on the (010) surface [see Fig. 1(d)] [12]. The unique feature of CeNiSn is that it has the nonsymmorphic glide and screw-axis symmetry (*Pnma* space group), which brings about such exotic electronic structures. Indeed a low-T resistivity plateau was observed in Sb-doped CeNiSn [13]. However, it has not been verified yet whether the resistivity plateau in CeNiSn at low T is really formed by the TSS. In addition, due to the nonsymmorphic glide and screw-axis symmetry of CeNiSn, the emergence of intriguing hourglass-type *bulk* band crossings and the consequent Dirac nodal-loop structures are predicted around the $\vec{k} = S$ point in the [100] Brillouin zone (BZ) boundary [14]. In order to prove whether CeNiSn really belongs to a TKI having the Möbius-twisted TSS as well as a Dirac semimetal having the hourglass-type *bulk* band crossings, it is essential to examine the electronic structure of CeNiSn via angle-resolved photoelectron spectroscopy (ARPES).

In this work, we have investigated the electronic structure of CeNiSn, which is a potential candidate of a TKI [12] as well as a Dirac nodal-loop semimetal [14]. We have performed ARPES measurements using synchrotron radiation. We have successfully measured Fermi surfaces (FSs) and band structures for three orthogonal crystallographic planes, which is important because the Möbius-twisted TSSs are predicted to be realized on the (010) surface [12] and the Dirac nodal-loop structures are expected to be in the [100] BZ boundary enclosing S [14]. Previously the ARPES study for the (101) surface of CeNiSn was reported [15], where the high-T Fermi surface and the effect of the anisotropic hybridization at low T in CeNiSn were discussed. Note that it is difficult to prepare the flat (100), (010), and (101) surfaces of CeNiSn because the natural cleavage plane of CeNiSn is the (101) plane [15–19]. We have also performed T-dependent ARPES measurements, and found that the behavior of Ce 4*f* ARPES is consistent with that of the Kondo resonance states having the Kondo temperature (T_K) of $T_K \sim 80$ K. This work demonstrates the

*Corresponding author: kangjs@catholic.ac.kr

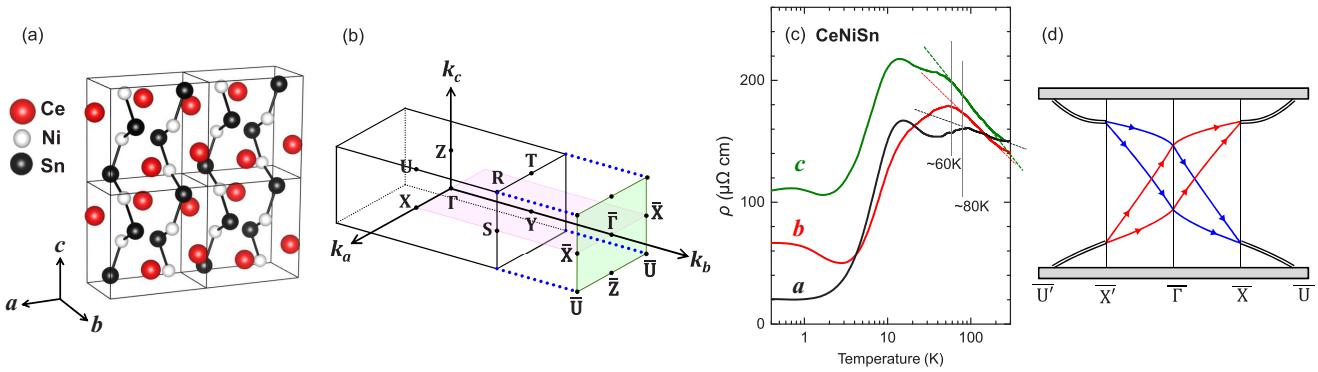

FIG. 1. Crystal structure and electrical resistivity of CeNiSn. (a) ϵ-TiNiSi-type orthorhombic crystal structure of CeNiSn. (b) The Brillouin zone (BZ) for the orthorhombic crystal structure, where the (010) surface BZ projected along k_b is marked in green. (c) T-dependent electrical resistivity $\rho(T)$ data of the purified single crystal of CeNiSn along a, b, and c directions [21,24]. (d) Two-dimensional (2D) plot of a pair of Möbius-twisted surface states on the (010) surface BZ, which is adopted from Ref. [12]. Here red and blue lines denote the states with positive and negative glide eigenvalues, respectively. Double lines along $\bar{X}\bar{U}$ and $\bar{X}'\bar{U}'$ denote the doubly degenerate surface states.

importance of the coherent Kondo states in determining the topological properties of CeNiSn.

II. EXPERIMENTAL DETAILS

A single-crystal ingot of CeNiSn was obtained by the Czochralski method using the tungsten crucible [20,21]. The pulling speed was 10–12 mm/hr. The furnace was filled with helium gas. A pipeline through which helium gas flowed was cooled by liquid nitrogen, which became a getter for impurity gasses contained in the helium gas. The ingot was annealed under a high vacuum of 10^{-9} Torr via the solid-state electrotransport method. The ingot was heated up to about 900 °C by flowing the DC current for the ingot under high vacuum for a period of about two weeks. According to the x-ray diffraction (XRD) data, CeNiSn crystallized in the orthorhombic ϵ-TiNiSn-type structure with the lattice constants of $a = 7.540$ Å, $b = 4.602$ Å, and $c = 7.614$ Å at $T \sim 300$ K [20].

ARPES measurements were carried out at the 4.0.3 beamline of the Advanced Light Source (ALS). The ARPES chamber is equipped with a Scienta $R4000$ electron analyzer with 0.1° angular resolution, and a vertical analyzer slit. Single-crystalline samples were cleaved *in situ* by using a blade-type cleaver, with Laue-assisted sample mounting to obtain (100), (010), (001), and (101) cleaved surfaces. Measurements were performed in vacuum better than 5×10^{-11} Torr and at ~20 K. The Fermi level (E_F) and the instrumental resolution of the system were determined from the Fermi-edge spectrum of evaporated Au. A total energy resolution (ΔE) of $\Delta E \approx 20$ meV was employed at the photon energy ($h\nu$) of $h\nu \sim 70$ eV. FS maps were obtained via polar rotations of the manipulator.

Band structure calculations were performed by employing the all-electron density functional theory (DFT) method, implemented in the full-potential local orbital (FPLO) code [22]. The generalized gradient approximation (GGA) is utilized for the DFT exchange-correlation functional [23], and the spin-orbit coupling (SOC) effect is included in the band calculations in a fully relativistic way.

III. RESULTS AND DISCUSSION

A. ARPES and hourglass-type band structures

Figure 1 shows the crystal structure and T dependence of the electrical resistivity $\rho(T)$ for CeNiSn. Figure 1(a) shows the ϵ-TiNiSi-type orthorhombic crystal structure of CeNiSn, where Ce, Ni, and Sn ions are denoted in red, gray, and black balls, respectively. Figure 1(b) shows the BZ for the orthorhombic crystal structure, where the (010) surface BZ, which is projected along k_b, is marked in green.

In Fig. 1(c) is shown the T dependence of the electrical resistivity $\rho(T)$ of CeNiSn along the a, b, and c directions [21,24]. As shown Fig. 1(c), the $\rho(T)$ data of purified single crystals of CeNiSn exhibit the characteristics of the coherent f-electron systems. That is, upon cooling, $\rho(T)$ increases and then decreases with maxima at certain T^*'s. Thus T^* can be considered as the coherence temperature T_{coh}. Due to the inherent anisotropic hybridization nature of CeNiSn, the observed T^* values are different: ~15 K along a and c, and ~50 K along b. Noteworthy is that, while ρ_b and ρ_c show the semiconducting nature at low T, ρ_a shows the semimetallic nature [21]. The Kondo temperature T_K can be determined from the logarithmic T dependence of $\rho(T)$ in the high-T side [25]. Since $\rho(T)$ deviates from the $-\ln(T)$ behavior below T_K [25,26], T_K values in CeNiSn are supposed to be ~80 K along a, ~70 K along b, and ~60 K along c [see Fig. 1(c)]. These T_K values are comparable to the previously estimated T_K's [27,28].

Chang *et al.* predicted that CeNiSn could belong to a new family of the topologically protected heavy-electron system having the Möbius-twisted surface states due to its nonsymmorphic crystal symmetry [12]. In Fig. 1(d) is shown the two-dimensional (2D) plot of a pair of the Möbius-twisted topological surface states (TSSs) on the (010) surface BZ schematically, which is adopted from Ref. [12]. Here red and blue lines correspond to the states with positive and negative glide eigenvalues, respectively. Double lines along $\bar{X}\bar{U}$ and $\bar{X}'\bar{U}'$ denote the doubly degenerate surface states due to a combination of time-reversal and glide symmetry. The Möbius character arises from the connectivity between Kramers pairs at $\bar{\Gamma}$ and $\bar{X}$ ($\bar{X}'$) points, and the hourglass

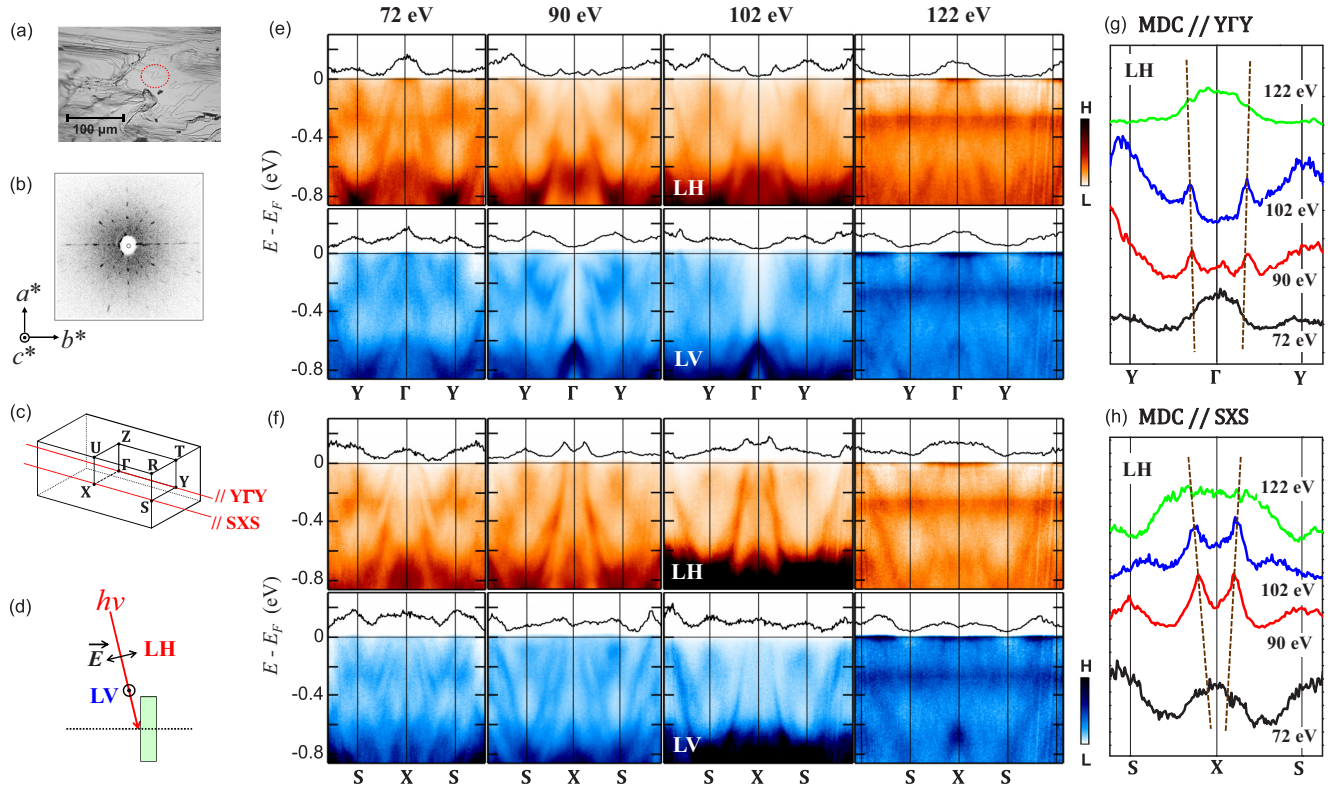

FIG. 2. ARPES data of CeNiSn for different $h\nu$'s. (a) The optical-microscopy (OM) image of a typical surface, which was measured after ARPES measurements were done. The size of the incident photon beam is drawn as a red dotted ellipse. (b) The Laue pattern of the (001) surface, for which ARPES measurements were done. (c) The 3D BZ of the orthorhombic CeNiSn with the $Y\Gamma Y$ and SXS symmetry lines being marked in red, along which ARPES data shown in (e) and (f) are obtained. (d) The schematic drawing of the ARPES measurement geometry with the linear horizontal (LH) polarization and the linear vertical (LV) polarization. (e), (f) The measured ARPES image plots of CeNiSn along $Y\Gamma Y$ and SXS, respectively, obtained with various $h\nu$'s of 72 eV, 90 eV, 102 eV, and 122 eV. The data in the top and bottom panels were obtained with the LH and LV polarizations, respectively. These data were obtained at $T \sim 20$ K. On top of each ARPES, the corresponding momentum distribution curve (MDC) at E_F is displayed. (g) Stack of the MDCs of the E_F states along $Y\Gamma Y$ from 72 eV to 122 eV, obtained with the LH polarization. (h) Similarly for the MDCs along SXS.

structure of the Möbius-twisted TSS contains two Dirac cones at the $\bar{\Gamma}$ point. The details of the Möbius-twisted TSSs are described in Ref. [12]. As shown in Fig. 1(d), the Möbius-twisted TSSs are expected to be observed along $\bar{X}\bar{\Gamma}\bar{X}'$ on the (010) surface BZ of CeNiSn.

Figure 2 shows the typical ARPES image plots of CeNiSn. An optical-microscopy (OM) image of a cleaved surface and the Laue pattern for the ARPES-studied surface are shown in Figs. 2(a) and 2(b), respectively. The red-dotted elliptical circle in Fig. 2(a) denotes the size of the incident photon beam, revealing that the ARPES and FS data, presented in this work, were obtained from the sufficiently flat region, corresponding to the well-defined surfaces. In order to check the orientation of the measured surfaces, Laue diffraction measurements were done before and after ARPES measurements. As an example, the measured Laue pattern for the (001) surface is shown in Fig. 2(b), which exhibits the twofold symmetry and confirms the measured surface to be the (001) plane. In Fig. 2(c), the symmetry lines along $Y\Gamma Y$ and SXS are marked in red in the three-dimensional (3D) orthorhombic BZ of CeNiSn. Figure 2(d) shows the schematic geometry for the ARPES measurements with the linear horizontal (LH) and the linear vertical (LV) polarizations, respectively. When photons are incident on a sample at a glancing angle, as shown in Fig. 2(d), the electric field ($\vec{E}$) is always parallel to the measured surface with the LV polarization, while $\vec{E}$ has both perpendicular and parallel components to the measured surface with the LH polarization.

Figures 2(e) and 2(f) present the ARPES image plots of CeNiSn along $Y\Gamma Y$ and SXS symmetry lines, respectively, obtained by varying $h\nu$'s from $h\nu = 72$ eV, 90 eV, 102 eV, and 122 eV. The ARPES images in the top panel were obtained with the LH polarization, and those in the bottom panel were obtained with the LV polarization. On top of each ARPES, the corresponding momentum distribution curve (MDC) at E_F is displayed. In all of them, very dispersive bands are observed, which arise mainly from Ni 3*d* states [14], and the observed features reveal the good quality of the measured ARPES data for CeNiSn. As will be confirmed in Fig. 3, these features indicate that they represent the intrinsic electronic structures of CeNiSn. The band shapes of these dispersive bands change with changing $h\nu$, reflecting the 3D electronic structure of CeNiSn. Significant variation in the highly dispersive bands is observed for the four different $h\nu$'s. This is also observed in the MDC stacks in Figs. 2(g) and 2(h), where the MDC peak positions vary with changing $h\nu$'s. This

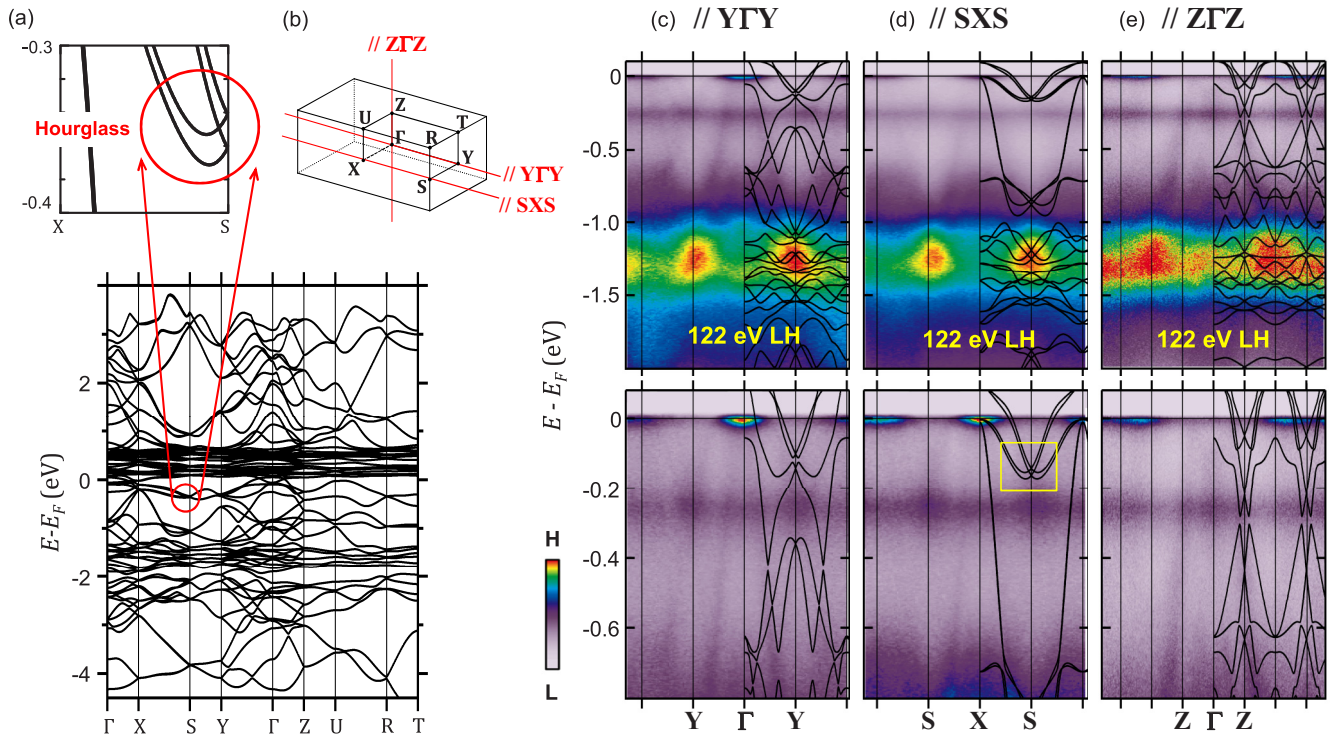

FIG. 3. DFT band structures and comparison with ARPES. (a) Calculated bulk band structures of CeNiSn along several high-symmetry lines, obtained in the DFT calculations. The zoomed-in view of a red circle shows the enlarged view of the hourglass-type bulk band structures near the S point. (b) 3D BZ of CeNiSn, where the high-symmetry lines denoted in red represent those along which ARPES spectra in (c)–(e) were obtained. (c) Top: The measured ARPES image plots along $Y\Gamma Y$ for the energy range of -2 eV $\leqslant E_i \leqslant E_F$, and the comparison with the calculated band structures on the right part. Bottom: The zoomed-out comparison for -0.8 eV $\leqslant E_i \leqslant E_F$ along $Y\Gamma Y$. (d), (e) Similarly along SXS and $Z\Gamma Z$, respectively. In these comparisons, the calculated band structures are shifted by $+0.2$ eV upward. Along SXS, a yellow box in the bottom panel denotes the hourglass-type bulk band structures predicted in the calculations. These data were obtained at $T \sim 20$ K.

reflects their 3D character, which is highlighted later in the $h\nu$-dependent E_F maps in Fig. 7. As discussed later, they do not correspond to the Möbius-twisted TSSs of the 2D character [12].

Note that the $h\nu = 122$ eV ARPES image plots appear quite different from those obtained at other $h\nu$'s. This is because Ce $4f$ emissions become strong at $h\nu = 122$ eV, which corresponds to the Ce $4d \rightarrow 4f$ resonance energy, while, at other $h\nu$'s, Ni $3d$ emissions are dominant [29]. At $h\nu = 122$ eV, two flat bands at E_F and at ~ -0.3 eV represent the Ce $4f$ Kondo states ($4f_{5/2}$ final states) and the spin-orbit (SO) split side bands ($4f_{7/2}$ final states), respectively. At $h\nu = 122$ eV, apart from two flat bands, highly dispersive bands are also observed, which exhibit similar features at other $h\nu$'s. This similarity suggests the existence of large hybridization between Ce $4f$ and Ni $3d$ states. We have compared the measured ARPES data with the DFT band calculations, and show them in Fig. 3. Figure 3(a) shows the calculated bulk band structures of CeNiSn along several high-symmetry lines, which were obtained in the DFT calculations. The flat bands near and above E_F up to ~ 0.5 eV correspond to Ce $4f$ states. The bands centered around -1.5 eV and the dispersive bands to E_F starting from these bands correspond to mainly Ni $3d$ states. It is seen that these dispersive Ni $3d$ states are hybridized with the Ce $4f$ states near E_F. In the zoomed-in view of the red circle in Fig. 3(a) is shown the hourglass-type bulk band structures near the S point. In Fig. 3(b) are shown the 3D BZ of orthorhombic CeNiSn schematically, where three symmetry lines are denoted in red, along which the measured ARPES images are compared with the calculated band structures in Figs. 3(c)–3(e).

The top panels of Figs. 3(c)–3(e) show the measured ARPES image plots of CeNiSn along $Y\Gamma Y$, SXS, and $Z\Gamma Z$, respectively, for the wide energy range (-2 eV $\leqslant E_i \leqslant E_F$). On the right parts of the figures, the measured ARPES images are compared with the corresponding calculated band structures. Similarly, the bottom panels of Figs. 3(c)–3(e) show the ARPES and their comparisons to the calculations for the narrow energy range (-0.8 eV $\leqslant E_i \leqslant E_F$). In the comparisons between ARPES and calculations, the calculated band structures are shifted by $+0.2$ eV upward [30]. As described in Fig. 2, the measured ARPES image plots reveal both the dispersive bands, having mainly the Ni $3d$ character, and the flat bands near E_F and ~ -0.3 eV, which have the Ce $4f$ character. The existence of light-mass Ni $3d$ hole-like bands dispersing from -1 eV and converging at E_F at Γ and X, and the existence of shallower electron bands with ~ -0.2 eV minima at Y and S are in reasonably good agreement between ARPES and the overplotted DFT bands in Figs. 3(c)–3(e). Note, however, that the Ce $4f$ SO-split side bands near -0.3 eV cannot be described by simple DFT calculations. For the description of these Kondo states, one needs to resort to using the dynamical mean-field theory (DMFT) band calculations, incorporating properly the Coulomb correlation of Ce $4f$ electrons [14].

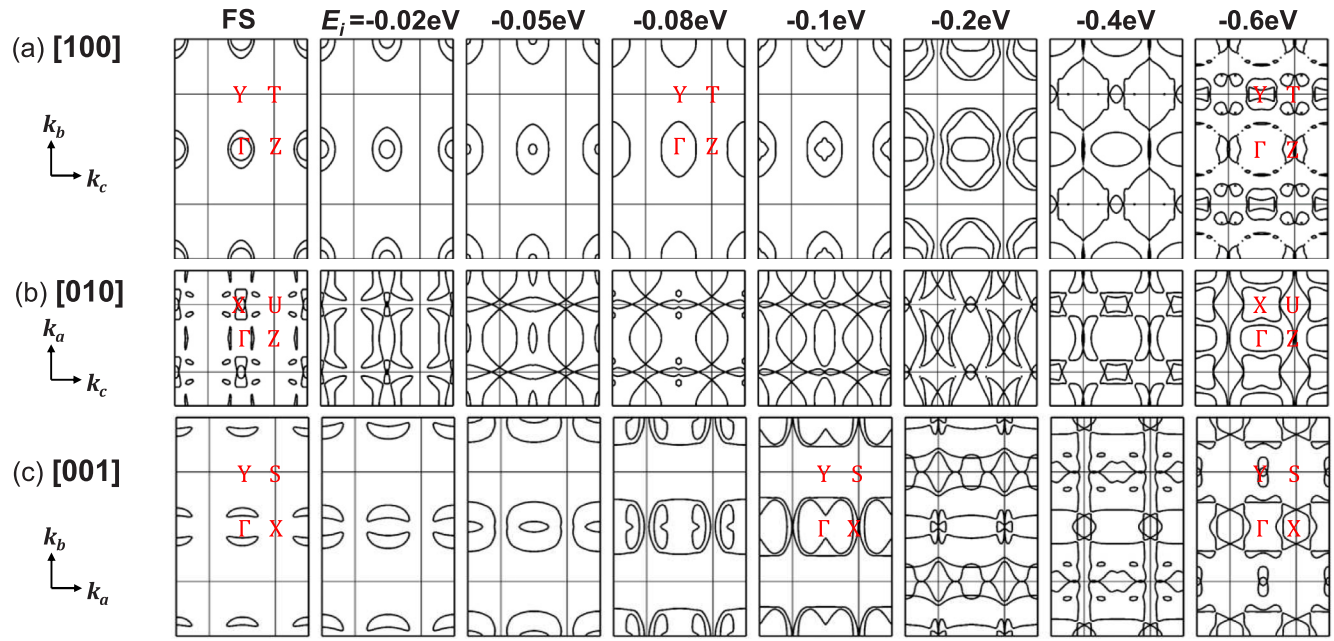

FIG. 4. Calculated Fermi surface (FS) and constant-energy (CE) contours of CeNiSn. (a) The calculated FS and CE contours on the [100] ($k_a = 0$) plane of CeNiSn, obtained from the density functional theory (DFT) calculations. The initial-state energy E_i for each CE contour is labeled on the top of each contour. (b) Similarly, for the [010] ($k_b = 0$) and [001] ($k_c = 0$) planes of CeNiSn. Here the BZs in all the FS/CE contours represent those of the orthorhombic BZs.

Figures 3(c)–3(e) show that the measured ARPES and the corresponding calculations along $Y\Gamma Y$, SXS, and $Z\Gamma Z$ agree reasonably well in the wide energy scale.

In Fig. 3(d) along SXS, a yellow box in the bottom panel denotes the hourglass-type bulk band structures predicted by the DFT band-structure calculations. In the DFT calculations for CeNiSn [14], there are hourglass-type bulk band crossings around the $\mathbf{k} = S$ point and the resulting Dirac nodal-loop structures enclosing S in the [100] BZ boundary. Both the hourglass-type band crossings [14] and the Möbius-twisted TSSs [12] arise from the nonsymmorphic glide and screw-axis symmetries (*Pnma* space group) of CeNiSn. Hence, it is significant to check experimentally the existence of the hourglass-type band crossings at low T. A Dirac nodal-loop semimetallic state having the hourglass-type band crossings is predicted to be an equilibrium state in the absence of coherent Ce 4f bands at high T, but the hourglass-type band crossings are predicted to survive even at low T [14]. In Fig. 3(d), the hourglass-type band crossings along SXS are not observed clearly in the measured ARPES images. On the other hand, there are some features near the expected hourglass structures with the energies and the slopes being similar to those of the DFT results. This finding, as well as the general agreement between ARPES and calculations in the wide energy scale, tends to imply that the hourglass-type bulk bands indeed exist along SXS in CeNiSn.

B. Constant-energy contours and Fermi surface

Figure 4 shows the calculated FS and constant-energy (CE) contours of CeNiSn. The 2D BZs in Fig. 4 represent those of three orthogonal [100] ($k_a = 0$), [010] ($k_b = 0$), and [001] ($k_c = 0$) planes of the orthorhombic structure. The initial-state energy (E_i) for each CE contour is labeled on the top of each contour. Figures 4(a) and 4(c) exhibit the twofold symmetry for the [100] and [001] planes, while Fig. 4(b) exhibits the nearly fourfold symmetry for the [010] plane, consistent with the lattice parameters of CeNiSn. The calculated FS and CE contours on the [100] plane of CeNiSn exhibit two FSs near the Γ point. With increasing $|E_i|$, the size of the inner CE decreases, while that of the outer CE increases, implying that the inner and outer FSs originate from an electron pocket and from a hole band, respectively. A similar trend is observed in the FS and CE contours on the [001] plane, implying that the inner FS has the electron character while the outer FS has the hole character. In contrast, FS and CE contours on the [010] plane exhibit rather complicated features.

In Fig. 5 are compared the measured and calculated FS and CE maps on the [010] plane of CeNiSn. The upper panel of Fig. 5 shows the measured CE maps on the [010] plane of CeNiSn with FS ($\equiv E_i = 0$ eV), $E_i = -0.1$ eV, -0.3 eV, -0.5 eV, and -0.7 eV, respectively, obtained at $h\nu = 122$ eV (the Ce 4f resonance) with the LH polarization and at $T =$ 20 K. The lower panel of Fig. 5 shows the DFT-calculated CE contours on the [010] plane of CeNiSn, cut at $E_i = -0.2$ eV, -0.3 eV, -0.5 eV, -0.7 eV, and -0.9 eV, respectively. In this comparison, we have compared the measured CEs with the calculated CEs that are shifted by -0.2 eV (corresponding to shifting E_F upward by $E' = E + 0.2$ eV). These shifts in the DFT-calculated CE maps yield a better agreement with the measured CE maps, as in the comparison between ARPES and the calculated band structures (see Fig. 3).

The trend in the measured CE maps with increasing $|E_i|$ is similar to that in the calculated CE maps. Furthermore, reasonably good agreement is found between the measured and calculated CE maps, near the Γ point (in the first BZ)

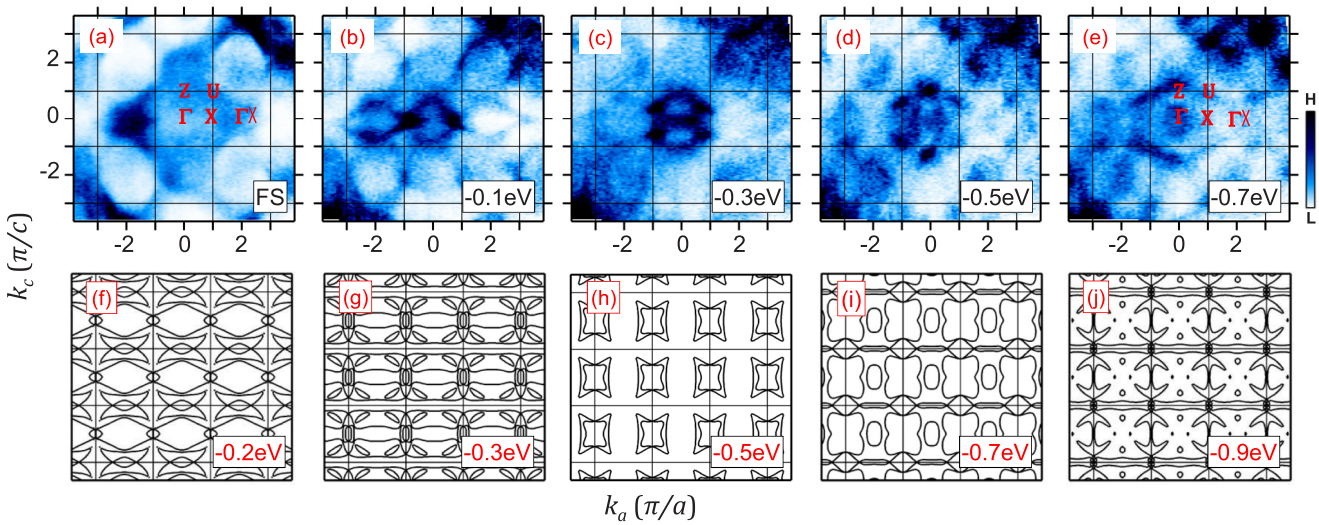

FIG. 5. Comparison of the measured and calculated FS and CE maps on the [010] ($k_b = 0$) plane of CeNiSn. Upper panels: The measured FS and CE maps with $E_i = 0$ eV ($\equiv$ FS), -0.1 eV, -0.3 eV, -0.5 eV, and -0.7 eV, respectively. These data were obtained at the Ce $4f$ resonance ($h\nu = 122$ eV) with the LH polarization and at $T = 20$ K. Lower panel: The DFT-calculated FS and CE contours, cut at $E_i = -0.2$ eV, -0.3 eV, -0.5 eV, -0.7 eV, and -0.9 eV, respectively. Black lines denote the BZs for the orthorhombic structure. In this comparison, the Fermi level (E_F) in the DFT calculations was shifted upward by 0.2 eV (i.e., $E' = E - 0.2$ eV). These data were obtained at $T \sim 20$ K.

for $E_i = 0$ eV, -0.1 eV, -0.5 eV, and -0.7 eV. These findings indicate that the measured CE maps are obtained from the proper (010) surface and that they represent the intrinsic features of the (010) surface. On the other hand, the features in the outer BZs (the second BZs surrounding the first BZ) in the measured CE maps appear different from those in the calculated CE maps. The major discrepancy is that the repeated features in the measured CE maps are larger than that expected for the orthorhombic BZ.

To understand the origin for such discrepancies, we have examined the DFT-calculated FS for the original orthorhombic structure and that unfolded into a larger BZ of the reduced Ce-only unit cell [31]. Since the FS and CEs in Fig. 5 were obtained at the Ce resonance energy, it is likely that they represent those by the Ce $4f$ states near E_F. Thus we have compared some of the measured $h\nu = 122$ eV FSs with the unfolded FSs in Fig. 6 by taking into account the effect of the reduced Ce-only unit cell. The left panel of Fig. 6(a) shows the measured FS on the [010] plane, obtained at the Ce $4f$ resonance ($h\nu = 122$ eV) with the LH polarization at $T = 20$ K. The right panel of Fig. 6(a) shows the DFT-calculated FS on the [010] plane, which is unfolded into a larger BZ (in red) of the Ce-only unit cell. The original orthorhombic BZ is denoted in black and that for the reduced Ce-only unit cell is denoted in red. The relation between the reduced Ce-only unit cell and the orthorhombic unit cell, the relation between the enlarged Ce-only BZ and the orthorhombic BZ, and the unfolded FS calculations are described in Ref. [31] (see Fig. 1, Fig. 6, and Fig. 7 in Ref. [31]). In this comparison, the calculated CE with $E_i = -0.1$ eV was chosen in both Figs. 6(a) and 6(b) because they yield good agreement with the measured FS and the amount of shift is similar to that employed in the ARPES comparison (+0.2 eV upward shift) (see Fig. 3). Indeed good agreement is found between the measured FS and the unfolded FS on the [010] plane, supporting that the discrepancy in the periodicity between the measured $h\nu = 122$ eV FS and the calculated FS for the orthorhombic BZ arises from the fact that the $h\nu = 122$ eV FS represents that due to the Ce $4f$ electrons. Similarly, in Fig. 6(b) are compared the measured FS on the [001] plane (left), obtained at $h\nu = 122$ eV with the LH polarization, with the unfolded DFT-calculated CE on the [001] plane in the enlarged Ce-only BZ (right). In this comparison, the calculated CE contour of $E_i = -0.1$ eV is chosen because the intensity of the calculated FS ($E_i = 0$ eV) is very weak. Similarly as for the [010] plane, a reasonably good agreement is found between the measured and the calculated FSs. From top to bottom in Fig. 6(c) are compared the Ce-only BZs on top of the [010] and the [001] orthorhombic BZ, respectively.

On the other hand, Ni $3d$ emissions are dominant away from the Ce $4f$ resonance, so that the measured FS away from the Ce $4f$ resonance is expected to represent that determined mainly by the Ni $3d$ states that cross E_F. Hence, we also compare the FS, obtained away from the Ce $4f$ resonance, with the DFT-calculated FS that is not unfolded into a Ce-only BZ. For this purpose, we have chosen $h\nu = 78$ eV FSs on the [101] plane, and show them in Fig. 6(e). The [101] plane, corresponding to the measured FS at $h\nu = 78$ eV [see Fig. 6(e)], is denoted in gray in the 3D orthorhombic BZ in Fig. 6(d). The left and right panels of Fig. 6(e) show the FS on the [101] plane, obtained at $h\nu = 78$ eV with the LV polarization, and the comparison between experiment and theory. Here the DFT-calculated FS (red curves) is superposed on the measured FS. The $h\nu = 78$ eV FS is similar to that in Ref. [15]. Since Ni $3d$ emissions are dominant at $h\nu = 78$ eV, the measured FS is expected to represent that determined mainly by the E_F-crossing Ni $3d$ states. Hence, in Fig. 6(e), the calculated FS is drawn for the orthorhombic structure and the BZ is not unfolded into a Ce-only BZ in contrast to the comparisons made in Figs. 6(a) and 6(b). This comparison

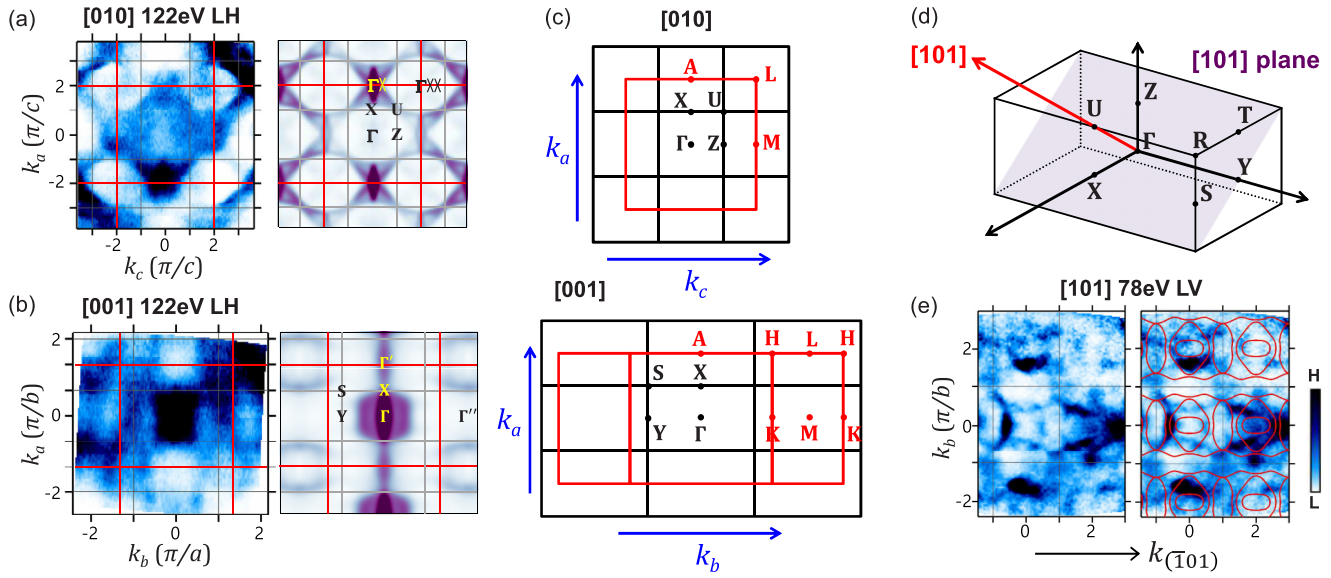

FIG. 6. Comparison of the measured FSs and the calculated FSs of CeNiSn. (a) Left: The measured FSs on the [010] ($k_b = 0$) plane, obtained at the Ce 4f resonance ($h\nu = 122$ eV) with the LH polarization. Right: The DFT-calculated FS on the [010] ($k_b = 0$) plane, which is unfolded into a larger BZ (in red) of the Ce-only unit cell [see top of (c)]. The original orthorhombic BZs are denoted in black. (b) Comparison of the FS on the [001] plane of CeNiSn, obtained at $h\nu = 122$ eV with the LH polarization, with the unfolded DFT-calculated CE on the [001] plane [see bottom of (c)]. Here the calculated CE contour of $E_i = -0.1$ eV is chosen. (c) Top: Comparison of the Ce-only BZ on top of the [010] orthorhombic BZ. Bottom: Similarly for the [001] plane. (d) The [101] plane corresponding to the measured FS shown in (e) is denoted in gray in the 3D orthorhombic BZ. (e) Left: The measured FS on the [101] plane, obtained at $h\nu = 78$ eV with the LV polarization. Right: Comparison of the measured FS with the DFT-calculated CE on the [101] plane, superposed onto each other. In this comparison, the calculated CE contour of $E_i = -0.2$ eV is chosen and the orthorhombic BZ is shown. All the FS data were obtained at $T = 20$ K.

reveals a reasonably good agreement between experiment and theory, confirming that the FS obtained at $h\nu = 78$ eV indeed represents that by the Ni 3d states and the intrinsic features of the (101) surface of CeNiSn.

C. Photon energy map and 3D electronic structures

Figure 7 shows the measured $h\nu$ maps of CeNiSn for FS and the initial-state energy (E_i) of $E_i = -0.5$ eV, obtained for $h\nu$ between 40 eV $\leqslant h\nu \leqslant$ 150 eV at $T = 20$ K with the LH polarization. Figure 7(a) shows the $h\nu$ axis and the measured plane by the $h\nu$ map, shown in Fig. 7(b), in the 3D orthorhombic BZ. These $h\nu$ maps cut through $Y\Gamma Y$, with the horizontal axis parallel to k_b ($\parallel k_{(010)}$) and the vertical $h\nu$ axis along k_c ($h\nu \parallel k_c$), so that the measured FS and CE contours represent those on the k_b-k_c plane ($\equiv$ [100] plane). The $h\nu$ map for the Fermi-edge state ($E_i = 0$ eV) corresponds to FS. The arcs in the $E_i = -0.5$ eV $h\nu$ map represent the corresponding $h\nu$'s. Similarly, Fig. 7(c) shows the $h\nu$ axis and the measured plane by the $h\nu$ map, shown in Fig. 7(d). These $h\nu$ maps cut through $Z\Gamma Z$, with the horizontal axis parallel to k_c ($\parallel k_{(001)}$) and the vertical $h\nu$ axis along k_b, so that the measured FS and CE contours also represent those on the k_c-k_b plane ([100] plane). In both Figs. 7(b) and 7(d), the BZ is calculated by using the inner potential of $V_0 = 12$ eV [32].

Note that these $h\nu$ maps in Figs. 7(b) and 7(d) are relevant to the confirmation of the Möbius-twisted TSSs, which are predicted to be within the very narrow region of the *bulk* insulating gap (in the k space) along $\bar{X}'\bar{\Gamma}\bar{X}$ in the (010) surface BZ, i.e., along $k_{(100)}$ in the (010) surface BZ [see Fig. 1(d)]. Namely, if there exist FSs arising from the TSSs on the (010) surface, straight line-like FSs are expected to be observed along k_b ($h\nu \parallel k_b$), indicating the 2D *surface* electronic structure of the Fermi-edge states. In the FS ($E_i = 0$ eV) in Fig. 7(b), a circular FS centered at the Γ point is observed, the size of which is found to increase with increasing $|E_i|$ (not shown here), implying its character to be the hole-pocket type FS. This argument is consistent with the observation of the increasing size of the FS centered at the Γ point in Fig. 7(d) for larger $|E_i|$. However, no straight line-like FSs are observed along k_b in both Figs. 7(b) and 7(d), suggesting that these Fermi-edge states correspond to the 3D bulk states. To summarize, the measured $h\nu$ maps for CeNiSn reveal that the metallic E_F-crossing states in the (010) surface BZ have the 3D nature, which seems to be against the 2D character of the predicted Möbius-twisted TSSs in CeNiSn.

D. T-dependent Ce 4f states and topological electronic structure

Figure 8(a) shows the angle-integrated survey photoemission spectroscopy (PES) spectra of CeNiSn, obtained at the Ce 4f on-resonance ($h\nu = 122$ eV) and well away from the resonance ($h\nu = 90$ eV), respectively. Clean Sn 4d core levels are observed around $\sim$−24 eV, which exhibit the spin-orbit (SO) split $4d_{5/2}$ and $4d_{3/2}$ peaks. This comparison shows clearly that both the Ce 4f states (in the valence band) and Ce 5p states ($\sim$−18 eV) are enhanced at $h\nu = 122$ eV due to the Ce $4d \rightarrow 4f$ resonance. The different line shapes of the valence-band spectra, obtained at $h\nu = 90$ eV and

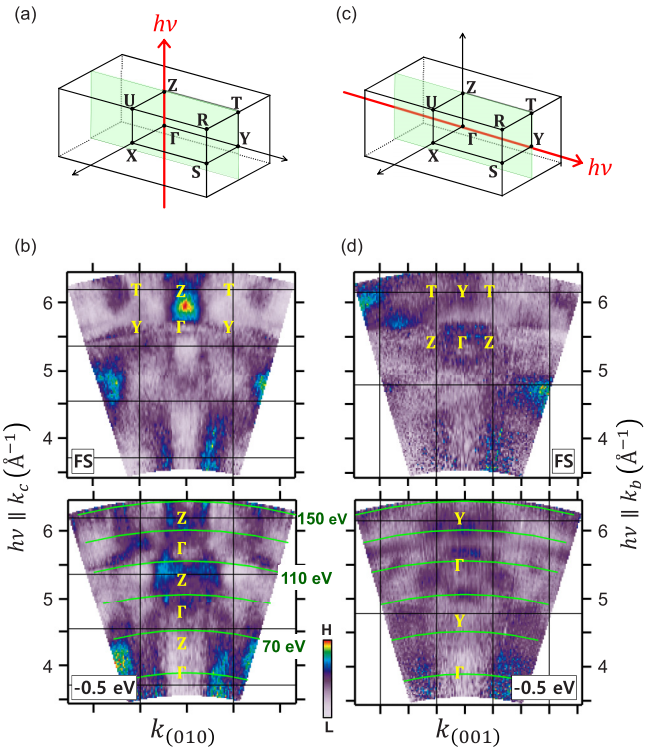

FIG. 7. The measured photon energy ($h\nu$) maps. (a) Schematic drawing for the $h\nu$ axis and the measured plane for the $h\nu$ map shown in (b), which are denoted in green in the 3D orthorhombic BZ. (b) The $h\nu$ maps with the horizontal axis $\parallel k_b$ and the vertical axis ($h\nu$) along k_c ($h\nu \parallel k_c$), which cut through $Y\Gamma Y$. The $h\nu$ map for the Fermi-edge state (FS: $E_i = 0$ eV) and that for the initial-state energy (E_i) of $E_i = -0.5$ eV are presented. (c) Schematic drawing of the measurement configuration for the $h\nu$ map in (d). (d) The $h\nu$ maps for FS and $E_i = -0.5$ eV, which cut through $Z\Gamma Z$ with the horizontal axis $\parallel k_c$ and the vertical axis ($h\nu$) along k_b ($h\nu \parallel k_b$). In both (b) and (d), the $h\nu$ maps were obtained for 40 eV $\leqslant h\nu \leqslant$ 150 eV with the LH polarization, and the BZ is calculated by using the inner potential of $V_0 = 12$ eV. The arcs in the $E_i = -0.5$ eV maps represent the corresponding $h\nu$'s. These data were obtained at $T \sim 20$ K.

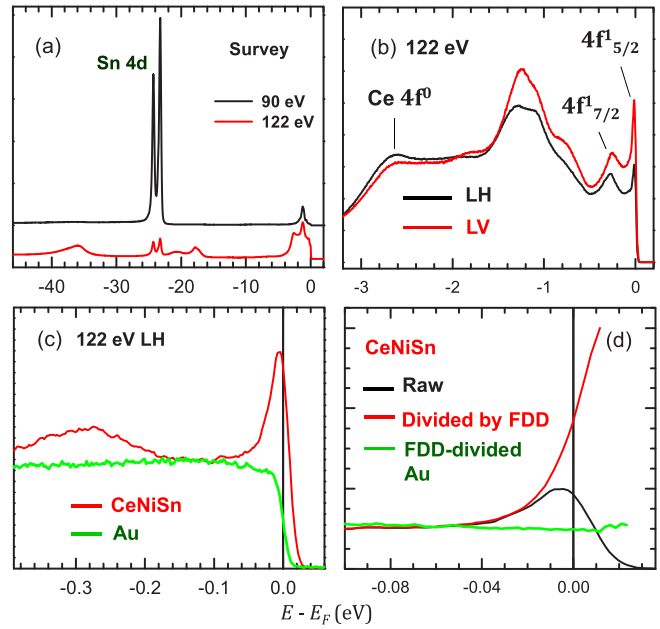

FIG. 8. Angle-integrated PES spectra of CeNiSn, measured $T \sim 20$ K. (a) Comparison of the survey PES spectra of CeNiSn, where Sn $4d$ core levels are included. They were obtained at the Ce $4f$ resonance ($h\nu = 122$ eV) and away from the Ce $4f$ resonance ($h\nu = 90$ eV), respectively. (b) Angle-integrated valence-band PES spectra of CeNiSn, obtained at the Ce $4f$ on resonance ($h\nu = 122$ eV) and with the linear horizontal (LH) polarization (black) and the linear vertical (LV) polarization (red), respectively. (c) The near-E_F PES spectrum of CeNiSn in comparison with that of Au as a Fermi-level reference. Both were obtained at 122 eV with the LH polarization and the experimental resolution of 20 meV ($\Delta E \approx 20$ meV). (d) Comparison of the near-E_F PES spectrum of CeNiSn before (black) and after (red) being divided by a broadened Fermi Dirac distribution (FDD) function with $T_{eff} = 60$ K. Green curve shows the Au spectrum divided by the FDD function.

$h\nu = 122$ eV, reveal that the Ce $4f$ states are located near E_F while most of the Ni $3d$ states are located around ~ -1.2 eV (see $h\nu = 90$ eV spectrum) [29]. Figure 8(b) shows the angle-integrated valence-band PES spectrum of CeNiSn, obtained at the Ce $4f$ on resonance ($h\nu = 122$ eV) with the LV polarization. The schematic geometry of the LV polarization measurement is shown in Fig. 2(c). The feature at ~ -1.2 eV represents the Ni $3d$ electron emission, which is supported by the $h\nu = 90$ eV spectrum in Fig. 8(a). As is typical in Ce systems, the Ce $4f$ PES emissions exhibit double-peak structures, one near E_F and the other at a deep binding energy (BE). The high-BE peak at ~ -2.5 eV represents the trivalent Ce $4f^1 \rightarrow 4f^0$ transition (a bare Ce $4f^0$ peak) [33,34]. The peak near E_F is the Kondo peak, corresponding to the $4f^1 \rightarrow 4f^1$ transition, arising from the hybridization between Ce $4f$ and conduction-band electrons [35–37]. The second peak at $E_i \sim -0.3$ eV is the Kondo sideband peak, corresponding to the SO-split $4f_{7/2}$ final state.

Figure 8(c) shows the near-E_F PES spectrum of CeNiSn, in comparison with a Fermi-level reference Au. Both were obtained at $h\nu = 122$ eV and at $T \approx 20$ K, which is below the estimated T_K's in Fig. 1(c). The same experimental resolution ($\Delta E \approx 20$ meV) was employed for these data. To determine the intrinsic density of states (DOS) near E_F for the Ce $4f$ states, we have divided the $h\nu = 122$ eV spectrum of CeNiSn by a broadened Fermi Dirac distribution (FDD) function, the results of which are shown in Fig. 8(d). As a reference, the Au spectrum divided by the FDD function is also shown in Fig. 8(d) (green curve), which reveals the flat DOS above E_F, in agreement with the expected DOS for Au. In contrast, the FDD-divided Ce $4f$ PES spectrum of CeNiSn exhibits an increasing DOS above E_F, confirming that the Ce $4f$ peak below E_F corresponds to the tail of the Kondo resonance peak that is located just above E_F [35,36]. Hence the analysis of the near-E_F spectrum of CeNiSn using the FDD function confirms the existence of the Ce $4f$ Kondo peak in CeNiSn. The Ce $4f$ Kondo peak clearly reveals the overall metallic bulk ground state of CeNiSn, consistent with its Kondo semimetallic nature. This feature also suggests that the region for the existence of the Möbius-twisted TSS in the k

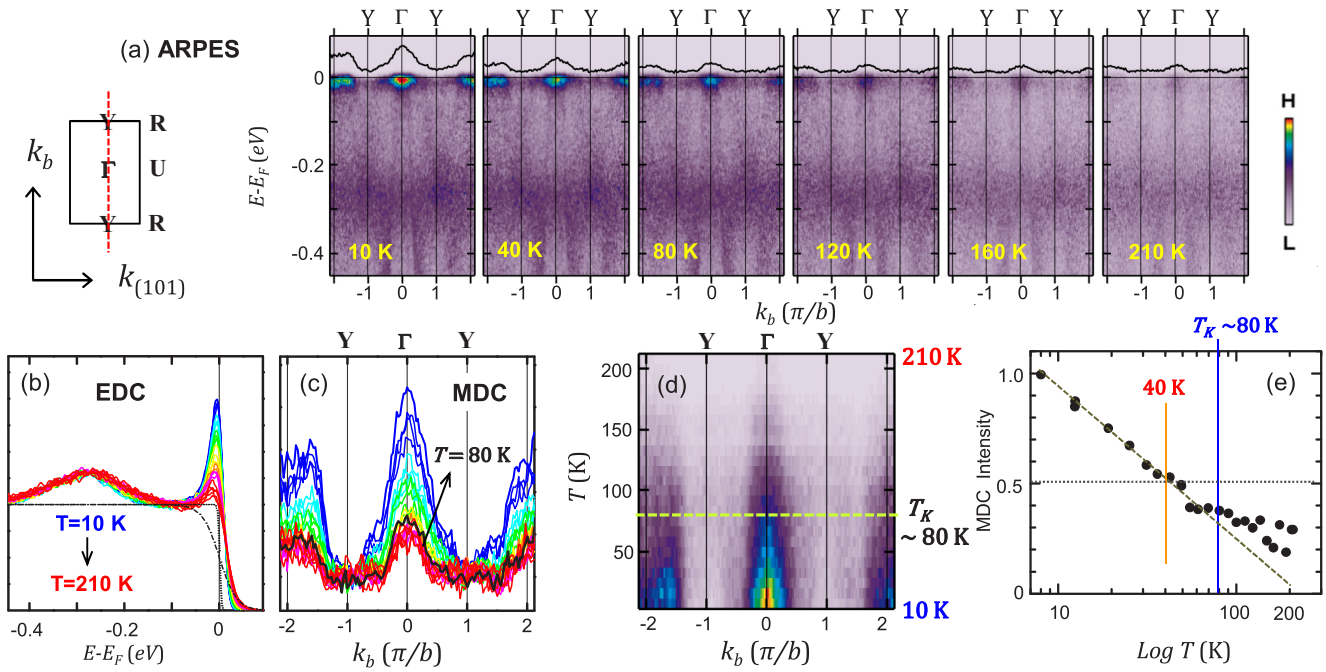

FIG. 9. T-dependent 4f states of CeNiSn. (a) Left: The schematic drawing of the symmetry line, along which ARPES data were obtained. It is denoted in red in the 2D orthorhombic BZ for the [101] plane. Right: The ARPES images along $Y\Gamma Y$ for selected temperatures. These were obtained at $h\nu = 122$ eV with the LH polarization. On top of each ARPES is displayed the corresponding MDC at E_F. (b) The T dependence of the angle-integrated energy distribution curves (EDCs) from 10 K to 210 K. (c) The T-dependent MDCs of the Fermi-edge states along $Y\Gamma Y$ from 10 K to 210 K. (d) The intensity plots of the MDCs of the Fermi-edge states along $Y\Gamma Y$ from 10 K to 210 K. (e) The intensity plot of the MDC peak at $k_b = 0$ of the Fermi-edge states vs log(T).

space could be very small. In other words, the bulk insulating region of CeNiSn in the k space would be very small. This finding makes it difficult to make a direct observation of the Möbius-twisted TSS experimentally.

We now discuss the T dependence of the Ce 4f Kondo states in CeNiSn, by showing the T-dependent ARPES of the Ce 4f states in Fig. 9. The left of Fig. 9(a) shows the 2D orthorhombic BZ for the [101] plane of CeNiSn, where the $Y\Gamma Y$ symmetry line is denoted in red, along which ARPES data were obtained. The right of Fig. 9(a) shows the ARPES image plots along $Y\Gamma Y$ for selected temperatures. All the ARPES data were obtained at Ce 4f resonance ($h\nu = 122$ eV) with the LH polarization. On top of each ARPES is displayed the corresponding MDC at E_F. The ARPES image plots exhibit a strong Fermi-edge peak near the Γ point at low T, which becomes weakened upon heating, and disappears finally. Figure 9(b) shows the angle-integrated energy distribution curves (EDCs) from 10 to 210 K. They reveal the T variation in the amplitude and width of the Ce 4f Kondo resonance states near E_F. With increasing T, the intensity of the Ce 4f Kondo peak decreases dramatically with the concomitant broadening of its energy width. This trend is similar to that of CeRhSb, an isostructural TKI candidate [31]. The additional broad feature at ~−0.3 eV represents a SO-split $4f_{7/2}$ final state (SO sideband peak), which is rather insensitive to T.

This behavior is shown clearly by plotting the MDCs of the Fermi-edge states along $Y\Gamma Y$. The MDC line cuts along $Y\Gamma Y$ from 10 K to 210 K are shown in Fig. 9(c) and the corresponding MDC images of the Fermi-edge states from 10 K to 210 K are shown in Fig. 9(d). The T-dependent variation of the MDCs of the Fermi-edge states manifests that, upon heating, the sharp peaks broaden into broad humps above $T \sim 80$ K, which is supported by the trend in the MDCs shown in Fig. 9(a). This finding indicates that the Ce 4f Kondo resonance states along $Y\Gamma Y$ are suppressed above ~80 K, suggesting that the Kondo temperature (T_K) is approximately 80 K.

This feature is seen more clearly in the intensity plot of the peak at $k_b = 0$ in the MDCs of the Fermi-edge states vs log(T) shown in Fig. 9(e). According to the impurity Kondo model, the Kondo resonance peak has the logarithmic dependence on T, the intensity of which falls to a half of the $T = 0$ K peak height at $T \approx 0.5T_K$ [38]. As shown in Fig. 9(e), the Kondo peak indeed reveals the logarithmic T dependence, and it becomes half at $T \sim 40$ K, yielding $T_K \approx 80$ K. This value of T_K is indeed consistent with those estimated from $\rho(T)$ data in Fig. 1(c). This feature also suggests that, due to the expected lower T_{coh} than T_K [T_{coh} was estimated to be ~15 K in Fig. 1(c)], it would be hard to clearly observe either the coherent hybridization gap that is to be formed below T_{coh} or the TSSs that are supposed to emerge inside the gap in the temperature range of the present ARPES measurement.

Finally, we would like to remark on the possible topological electronic structure of CeNiSn. In this work, we have succeeded in obtaining the intrinsic FS and ARPES data for three orthogonal planes of CeNiSn. The measured ARPES data reveal the dispersive bands of mainly Ni 3d character and the flat Ce 4f Kondo resonance. However, in the measured ARPES data for CeNiSn (see Fig. 2), no Möbius-twisted TSSs are observed, which appears to be inconsistent with the

topological nature of CeNiSn. Nonetheless, the missing TSSs are not against the prediction of CeNiSn being a possible TKI because the Möbius-twisted TSSs might exist within the very small bulk energy gap near E_F as well as within the very narrow region of the bulk insulating gap in the k space along $k_{(100)}$ in the (010) surface BZ. On the other hand, the weak features of the hourglass-type bulk band crossings are observed along SXS in the ARPES images on the [100] BZ boundary plane, with the energies and the slopes being similar to those in the DFT calculations (see Fig. 3), which provides some evidence for the Dirac nodal-loop semimetallic nature of CeNiSn and serves as a positive step for CeNiSn being a possible TKI. In order to confirm the existence of the TSSs in CeNiSn, the state-of-the-art ARPES experiment would be required, which satisfies the experimental conditions of the exposure of the perfectly flat plane, very low temperature, and very high energy resolution. Above all, it is important to prepare the flat (010) surface plane of CeNiSn, which is difficult because the easy cleavage plane of CeNiSn is the (101) surface plane [19].

IV. CONCLUSION

By employing T-dependent ARPES, the electronic structure of a potential TKI candidate and a Dirac nodal-loop semimetal CeNiSn has been investigated. We have successfully measured the FSs and the band structures of CeNiSn for three orthogonal crystallographic planes. The very dispersive bands of mainly Ni $3d$ character and the flat Ce $4f$ Kondo resonance are observed. The measured FSs and ARPES bands agree well with the DFT calculations, indicating that the measured FSs and ARPES band structures are intrinsic to CeNiSn. The Fermi-state $h\nu$ map on the k_c-k_b plane (with the vertical $h\nu$ axis along k_b) reveals the 3D character for the metallic E_F-crossing states, which refutes the observed E_F-crossing metallic states being the Möbius-twisted TSSs of the 2D character on the (010) surface. Nevertheless, the weak features of the hourglass-type *bulk* band crossings are observed along SXS in the ARPES images, with the energies and slopes being similar to those in the DFT calculations. This finding provides a positive step toward the investigation of the TKI nature of CeNiSn with the state-of-the-art ARPES experiment. In the T-dependent Ce $4f$ ARPES measurement, the Ce $4f$ Kondo resonance states are observed at low T, which become weak with increasing T and vague above ~80 K, consistent with the T_K values of CeNiSn estimated from $\rho(T)$ data. This work suggests the importance of the coherent Kondo states in determining the topological properties of CeNiSn.

ACKNOWLEDGMENTS

This work was supported by the National Research Foundation (NRF) of Korea (Grant No. 2019R1A2C1004929). The ALS is supported by US DOE under Contract No. DE-AC02-05CH11231. K.K. is supported by the internal R&D program at KAERI (Grant No. 524460-23) and NRF (Grant No. 2016R1D1A1B02008461).

[1] M. Z. Hasan and C. L. Kane, Colloquium: Topological insulators, Rev. Mod. Phys. **82**, 3045 (2010).
[2] X.-L. Qi and S.-C. Zhang, Topological insulators and superconductors, Rev. Mod. Phys. **83**, 1057 (2011).
[3] M. Dzero, K. Sun, V. Galitski, and P. Coleman, Topological Kondo Insulators, Phys. Rev. Lett. **104**, 106408 (2010).
[4] M. Dzero, K. Sun, P. Coleman, and V. Galitski, Theory of topological Kondo insulators, Phys. Rev. B **85**, 045130 (2012).
[5] S. Wolgast, C. Kurdak, K. Sun, J. W. Allen, D.-J. Kim, and Z. Fisk, Low-temperature surface conduction in the Kondo insulator SmB_6, Phys. Rev. B **88**, 180405(R) (2013).
[6] Z.-H. Zhu, A. Nicolaou, G. Levy, N. P. Butch, P. Syers, X. F. Wang, J. Paglione, G. A. Sawatzky, I. S. Elfimov, and A. Damascelli, Polarity-Driven Surface Metallicity in SmB_6, Phys. Rev. Lett. **111**, 216402 (2013).
[7] D. J. Kim, J. Xia, and Z. Fisk, Topological surface state in the Kondo insulator samarium hexaboride, Nat. Mater. **13**, 466 (2014).
[8] G. Li, Z. Xiang, F. Yu, T. Asaba, B. Lawson, P. Cai, C. Tinsman, A. Berkley, S. Wolgast, Y. S. Eo, D.-J. Kim, C. Kurdak, J. W. Allen, K. Sun, X. H. Chen, Y. Y. Wangm Z. Fisk, and Lu Li, Two-dimensional Fermi surfaces in Kondo insulator SmB_6, Science **346**, 1208 (2014).
[9] N. Xu, P. K. Biswas, J. H. Dil, R. S. Dhaka, G. Landolt, S. Muff, C. E. Matt, X. Shi, N. C. Plimb, M. Radović, E. Pomjakushina, K. Conder, A. Amato, S. V. Borisenko, R. Yu, H.-M. Weng, Z. Fang, X. Dai, J. Mesot, H. Ding, and M. Shi, Direct observation of the spin texture in strongly correlated SmB_6 as evidence of the topological Kondo insulator, Nat. Commun. **5**, 4566 (2014).
[10] B. S. Tan, Y.-T. Hsu, B. Zeng, M. C. Hatnean, N. Harrison, Z. Zhu, M. Hartstein, M. Kiourlappou, A. Sirvastava, M. D. Johannes, T. P. Murphy, J.-H. Park, L. Balicas, G. G. Lonzarich, G. Balakrishnan, and S. E. Sebastian, Unconventional Fermi surface in an insulating state, Science **349**, 287 (2015).
[11] P. Hlawenka, K. Siemensmeyer, E. Weschke, A. Varykhalov, J. Sánchez-Barriga, N. Y. Shitsevalova, A. V. Dukhnenko, V. B. Filipov, S. Gabáni, K. Flachbart, O. Rader, and E. D. L. Rienks, Samarium hexaboride is a trivial surface conductor, Nat. Commun. **9**, 517 (2018).
[12] P.-Y. Chang, O. Erten, and P. Coleman, Möbius Kondo insulators, Nat. Phys. **13**, 794 (2017).
[13] A. Ślebarski and J. Spalek, From Kondo semimetal to spin-glass behavior in doped $CeNi_{1-\delta}Sn_{1+\delta-\chi}Sb_\chi$ system, Philos. Mag. **89**, 1845 (2009).
[14] T.-S. Nam, C.-J. Kang, D.-C. Ryu, J. Kim, H. Kim, K. Kim, and B. I. Min, Topological bulk band structures of the hourglass and Dirac nodal-loop types in Ce Kondo systems: CeNiSn, CeRhAs, and CeRhSb, Phys. Rev. B **99**, 125115 (2019).
[15] C. Bareille, T.-S. Nam, T. Takabatake, K. Kuroda, T. Yajima, M. Nakayama, S. Kunisada, S. Akebi, M. Sakano, S. Sakuragi, R. Noguchi, B. I. Min, S. Shin, and T. Kondo, Strongly anisotropic high-temperature Fermi surface of the Kondo semimetal CeNiSn revealed by angle-resolved photoemission spectroscopy, Phys. Rev. B **100**, 045133 (2019).
[16] O. Janka, O. Niehaus, R. Pöttgen, and B. Chevalier, Cerium intermetallics with TiNiSi-type structure, Z. Naturforsch. B **71**, 737 (2016).

[17] U. Vaknin, D. Shermana, and S. Gorfman, Geometrical prediction of cleavage planes in crystal structures, IUCrJ **8**, 793 (2021).

[18] According to the repeated cleaving of CeNiSn crystals, we have found that the easy cleavage plane of CeNiSn is (101).

[19] S. Seong and J.-S. Kang, Angle-resolved photoemission spectroscopy study of the (101) surface of the Kondo insulator CeNiSn, Curr. Appl. Phys. **41**, 207 (2022).

[20] Y. Onuki, M. Kakihana, M. Hedo, and T. Nakama, High-quality single crystal growth in heavy fermion compounds, in *Crystal Growth of Intermetallics*, edited by P. Gille and Y. Grin (Walter de Gruyter, Berlin, 2019), pp. 189–215.

[21] G. Nakamoto, T. Takabatake, H. Fujii, A. Mimami, K. Maezawa, I. Oguro, and A. A. Menovsky, Crystal growth and characterization of the Kondo semimetal CeNiSn, J. Phys. Soc. Jpn. **64**, 4834 (1995).

[22] K. Koepernik and H. Eschrig, Full-potential nonorthogonal local-orbital minimum-basis band-structure scheme, Phys. Rev. B **59**, 1743 (1999).

[23] J. P. Perdew, K. Burke, and M. Ernzerhof, Generalized Gradient Approximation Made Simple, Phys. Rev. Lett. **77**, 3865 (1996).

[24] T. Takabatake, G. Nakamoto, T. Yoshino, H. Fujii, K. Izawa, S. Nishigori, H. Goshima, T. Suzuki, T. Fujita, K. Maezawa, T. Hiraoka, Y. Okayama, I. Oguro, A. A. Menovsky, K. Neumaier, A. Brückl, and K. Andres, Localization effects in Kondo semimetals CeNiSn and CeRhSb, Phys. B: Condens. Matter **223-224**, 413 (1996).

[25] R. M. White, *Quantum Theory of Magnetism*, Solid-State Sciences, Vol. 32 (Springer-Verlag, Berlin, 1983).

[26] S. Jang, J. D. Denlinger, J. W. Allen, V. S. Zapf, M. B. Maple, J. N. Kim, B. G. Jang, and J. H. Shim, Evolution of the Kondo lattice electronic structure above the transport coherence temperature, Proc. Natl. Acad. Sci. USA **117**, 23467 (2020).

[27] S. Nishigori, H. Goshima, T. Suzuki, T. Fujita, G. Nakamoto, H. Tanaka, T. Takabatake, and H. Fujii, Pseudogap due to Coherence Kondo effect in CeNiSn and CeRhSb, J. Phys. Soc. Jpn. **65**, 2614 (1996).

[28] T. Takabatake, T. Sasakawa, J. Kitagawa, T. Suemitsu, Y. Echizen, K. Umeo, M. Sera, and Y. Bando, Thermoelectric properties of Ce-based Kondo semimetals and semiconductors, Phys. B: Condens. Matter **328**, 53 (2003).

[29] J. J. Yeh and I. Lindau, Atomic subshell photoionization cross sections and asymmetry parameters: $1 \leqslant Z \leqslant 103$, At. Data Nucl. Data Tables **32**, 1 (1985).

[30] Such a shift reflects the uncertainty in determining the Fermi level (E_F) in DFT calculations. We have used the same shifts in both FS and ARPES comparisons.

[31] S. Seong, K. Kim, E. Lee, C.-J. Kang, T. Nam, B. I. Min, T. Yoshino, T. Takabatake, J. D. Denlinger, and J.-S. Kang, Angle-resolved photoemission spectroscopy study of the Möbius Kondo insulator candidate CeRhSb, Phys. Rev. B **100**, 035121 (2019).

[32] In determining the magnitude of the inner potential (V_0), we looked for V_0, for which the periodic features along $h\nu$ matches the size of the BZ along k_c. Based on this criterion, $V_0 = 12$ eV was chosen for CeNiSn.

[33] P. A. Cox, Y. Baer, and C. K. Jørgesen, The coefficients of fractional parentage for ionization of partly filled f shells compared with photoelectron spectra of lanthanide compounds and metals, Chem. Phys. Lett. **22**, 433 (1973); P. A. Cox, Fractional parentage methods for ionisation of open shells of d and f electrons, Struc. Bond. **24**, 59 (1975).

[34] F. Gerken, A. S. Flodstrom, J. Barth, L. I. Johnsson, and C. Kunz, Surface core level shifts of the lanthanide metals Ce^{58}-Lu^{71}: A comprehensive experimental study, Phys. Scr. **32**, 43 (1985).

[35] O. Gunnarsson and K. Schönhammer, Electron spectroscopies for Ce compounds in the impurity model, Phys. Rev. B **28**, 4315 (1983); Double occupancy of the *f* orbitals in the Anderson model for Ce compounds, **31**, 4815 (1985); *Handbook on the Physics and Chemistry of Rare Earths*, edited by K. A. Gschneidner, L. Eyring, and S. Hüfner (North Holland, Amsterdam, 1987), Vol. 10, p. 103.

[36] J. W. Allen, S.-J. Oh, O. Gunnarsson, K. Schönhammer, M. B. Maple, M. S. Torikachvili, and I. Lindau, Electronic structure of cerium and light rare-earth intermetallics, Adv. Phys. **35**, 275 (1986).

[37] B. I. Min, H. J. F. Jansen, T. Oguchi, and A. J. Freeman, Local-density total-energy supercell description of excited-state properties of solids: Ce photoemission and inverse photoemission spectra, Phys. Rev. B **33**, 8005 (1986).

[38] T. A. Costi, Kondo Effect in a Magnetic Field and the Magnetoresistivity of Kondo Alloys, Phys. Rev. Lett. **85**, 1504 (2000).